RESEARCH ARTICLE

QUANTUM SIMULATION

Observation of generalized *t-J* spin dynamics with tunable dipolar interactions

Annette N. Carroll[1]*, Henrik Hirzler[1]†, Calder Miller[1], David Wellnitz[1], Sean R. Muleady[1,2], Junyu Lin[1], Krzysztof P. Zamarski[1,3], Reuben R. W. Wang[1]‡§, John L. Bohn[1], Ana Maria Rey[1], Jun Ye[1]*

Long-range and anisotropic dipolar interactions profoundly modify the dynamics of particles hopping in a periodic lattice potential. We report the realization of a generalized *t-J* model with dipolar interactions using a system of ultracold fermionic molecules with spin encoded in the two lowest rotational states. We independently tuned the dipolar Ising and spin-exchange couplings and the molecular motion and studied their interplay on coherent spin dynamics. Using Ramsey spectroscopy, we observed and modeled interaction-driven contrast decay that depends strongly both on the strength of the anisotropy between Ising and spin-exchange couplings and on motion. This study paves the way for future exploration of kinetic spin dynamics and quantum magnetism with highly tunable molecular platforms in regimes that are challenging for existing numerical and analytical methods.

The *t-J* model, which arises from the more general Fermi-Hubbard model in the limit of large onsite interactions U, fundamentally describes a competition between motion via tunneling between lattice sites, t, and spin interactions, J, caused by superexchange through virtual tunneling of particles in adjacent lattice sites. The model has long been proposed to explain unconventional phases, including high-temperature superconductivity (*1*–*3*). Ultracold atoms with contact interactions have recently emerged as a controllable system to study the behavior of this model, but the $J \sim t^2/U$ scaling of superexchange has limited the range of accessible phases to $J \ll t$ and imposes stringent low temperature requirements to observe interaction-induced phase transitions (*4*–*6*).

Adding long-range anisotropic dipolar interactions, where J can be tuned independently of t, softens the low-temperature constraints on phase transitions and generates a generalized *t-J* model that is predicted to produce exotic phases, including an enhanced superfluid state (*7*, *8*). Magnetic atoms provide access to dipolar interactions that, while relatively weak, have recently produced a variety of quantum phase transitions (*9*, *10*) and out-of-equilibrium spin dynamics in optical lattices (*11*–*15*). Ultracold polar molecules offer the advantage of stronger, tunable dipolar interactions (*16*–*21*). With electric field ($\boldsymbol{E}$)–tunable interactions between pseudo-spins encoded in rotational states, effective spin and spin-motion models can be implemented with high controllability (*22*) if two-body loss is suppressed by either strong confinement into lower dimensions (*23*) or collisional shielding with microwaves (*24*–*30*) or static electric fields (*31*–*35*). The extended lifetime of these itinerant molecules enables the combination of motion and strong dipolar interactions to study exotic spin-motion phenomena. Here, we report the realization of a generalized *t-J* model using ultracold dipolar molecules and the exploration of the system's out-of-equilibrium dynamics with independent control over both the motion and the interaction anisotropy $\chi = J_Z - J_\perp$ between spin-exchange ($J_\perp$) and Ising (J_Z) couplings in an XXZ spin model.

Dipolar interactions between molecules in optical lattices

We prepared degenerate gases of ^{40}K and ^{87}Rb in a crossed optical dipole trap and loaded these atoms into the ground band of a three-dimensional (3D) lattice with spacing a_y = 540 nm in the vertical direction and $a_x = a_z$ = 532 nm in the horizontal directions. The atoms were then converted to fermionic KRb molecules (*36*) in their rovibrational ground state $|0\rangle$, where $|N\rangle$ is the rotational state with $\boldsymbol{E}$-dressed quantum number N and projection $m_N = 0$ onto the quantization axis set by $\boldsymbol{E}$. The highest observed average molecular filling fraction was about 13%. For the spin measurements throughout this work, we used the two lowest rotational states of the molecule $|0\rangle$ and $|1\rangle$ as our spin-1/2 manifold, referred to as $|\downarrow\rangle$ and $|\uparrow\rangle$, respectively.

Heteronuclear molecules intrinsically have field-tunable dipolar interactions. The rotational states have induced dipole moments $d_\downarrow = \langle\downarrow|d_y|\downarrow\rangle$ and $d_\uparrow = \langle\uparrow|d_y|\uparrow\rangle$ and transition dipole moment $d_{\downarrow\uparrow} = \langle\downarrow|d_y|\uparrow\rangle$, where d_y is the dipole operator along $\hat{y}$, the quantization axis set by $\boldsymbol{E}$. These dipole moments depend on $|\boldsymbol{E}|$, with $d_\downarrow \approx d_\uparrow \approx 0$ at $|\boldsymbol{E}| \approx 0$ and $|d_\downarrow|, |d_\uparrow| > 0$ at $|\boldsymbol{E}| > 0$, as other rotational states get mixed into the field-dressed state $|N\rangle$. The dipolar interactions and the motional confinement provided by optical lattices are illustrated in Fig. 1, A and B.

Dipolar interactions are described by

$$\hat{H}_{\text{int}} = h\int d^3\boldsymbol{r}\int d^3\boldsymbol{r}'\frac{[1-3\cos^2(\theta)]a_x^3}{2|\boldsymbol{r}-\boldsymbol{r}'|^3}\times \left\{\begin{array}{l}\frac{J_\perp}{2}\left[\hat{s}^+(\boldsymbol{r})\hat{s}^-(\boldsymbol{r}')+\hat{s}^+(\boldsymbol{r}')\hat{s}^-(\boldsymbol{r})\right]+J_Z\hat{s}^Z(\boldsymbol{r})\hat{s}^Z(\boldsymbol{r}')+\\ V\hat{n}(\boldsymbol{r})\hat{n}(\boldsymbol{r}')+W\left[\hat{n}(\boldsymbol{r})\hat{s}^Z(\boldsymbol{r}')+\hat{s}^Z(\boldsymbol{r})\hat{n}(\boldsymbol{r}')\right]\end{array}\right\} \quad (1)$$

where $\hat{\psi}_\sigma(\boldsymbol{r})$ is the fermionic field operator at position $\boldsymbol{r}$ with spin σ (*7*, *8*, *36*), $\hat{n}(\boldsymbol{r}) = \sum_\sigma \hat{\psi}_\sigma^\dagger(\boldsymbol{r})\hat{\psi}_\sigma(\boldsymbol{r})$ is the density, $\hat{s}^Z(\boldsymbol{r}) = \left[\hat{\psi}_\uparrow^\dagger(\boldsymbol{r})\hat{\psi}_\uparrow(\boldsymbol{r}) - \hat{\psi}_\downarrow^\dagger(\boldsymbol{r})\hat{\psi}_\downarrow(\boldsymbol{r})\right]/2$ is the local magnetization, and $\hat{s}^+(\boldsymbol{r}) = \hat{\psi}_\uparrow^\dagger(\boldsymbol{r})\hat{\psi}_\downarrow(\boldsymbol{r})$ ($\hat{s}^-(\boldsymbol{r}) = \left[\hat{s}^+(\boldsymbol{r})\right]^\dagger$) raises (lowers) the spin. θ is the angle between $\boldsymbol{E}$ and $\boldsymbol{r}-\boldsymbol{r}'$. $hJ_\perp = 2d_{\downarrow\uparrow}^2/\left(4\pi\epsilon_0 a_x^3\right)$ is the spin-exchange interaction, $hJ_Z = \left(d_\downarrow - d_\uparrow\right)^2/\left(4\pi\epsilon_0 a_x^3\right)$ is the Ising interaction arising from differential dipole moments of the two states, $hV = \left(d_\downarrow + d_\uparrow\right)^2/\left(16\pi\epsilon_0 a_x^3\right)$ is the density-density interaction due to average dipole moments, and $hW = \left(d_\uparrow^2 - d_\downarrow^2\right)/\left(8\pi\epsilon_0 a_x^3\right)$ is the residual spin-density interaction arising from the cross-term of differential and average dipole moments. The relationship between dipole moments and $J_\perp$, J_Z, V, and W is illustrated in Fig. 1C. The full Hamiltonian is $\hat{H} = \hat{H}_{\text{sp}} + \hat{H}_{\text{int}}$ (*36*), where $\hat{H}_{\text{sp}} = \int d^3\boldsymbol{r}\sum_\sigma \hat{\psi}_\sigma^\dagger(\boldsymbol{r})H_0\hat{\psi}_\sigma(\boldsymbol{r})$ and $H_0 = -\frac{\hbar^2}{2m}\nabla^2 + \sum_{\alpha=x,y,z} V_{\text{L},\alpha}\sin^2\left(\frac{\pi r_\alpha}{a_\alpha}\right)$ describe the kinetic and lattice potential energies, respectively (for simplicity, we neglect an external confining potential). Here, $\hbar = h/2\pi$ is the reduced Planck constant, m is the mass of ^{40}K^{87}Rb, and $V_{\text{L},\alpha}$ is lattice depth in the $\alpha \in (x, y, z)$ direction.

In a deep 3D optical lattice, molecules cannot move, and the Hamiltonian becomes a spin model of frozen dipoles. In contrast, in the absence of horizontal lattices ($V_{\text{L},x} = V_{\text{L},z} = 0$), molecules are fully itinerant, so the Hamiltonian describes quasi-2D dipolar collisions

[1]JILA, National Institute of Standards and Technology, and Department of Physics, University of Colorado, Boulder, CO, USA. [2]Joint Center for Quantum Information and Computer Science, Joint Quantum Institute, National Institute of Standards and Technology, and University of Maryland, College Park, MD, USA. [3]Institut für Experimentalphysik und Zentrum für Quantenphysik, Universität Innsbruck, Innsbruck, Austria.
*Corresponding author. Email: annette.carroll@colorado.edu (A.N.C.); ye@jila.colorado.edu (J.Y.)
†Present address: Institute for Quantum Electronics, ETH Zürich, Zürich, Switzerland.
‡Present address: ITAMP, Center for Astrophysics | Harvard & Smithsonian, Cambridge, MA, USA.
§Present address: Department of Physics, Harvard University, Cambridge, MA, USA.

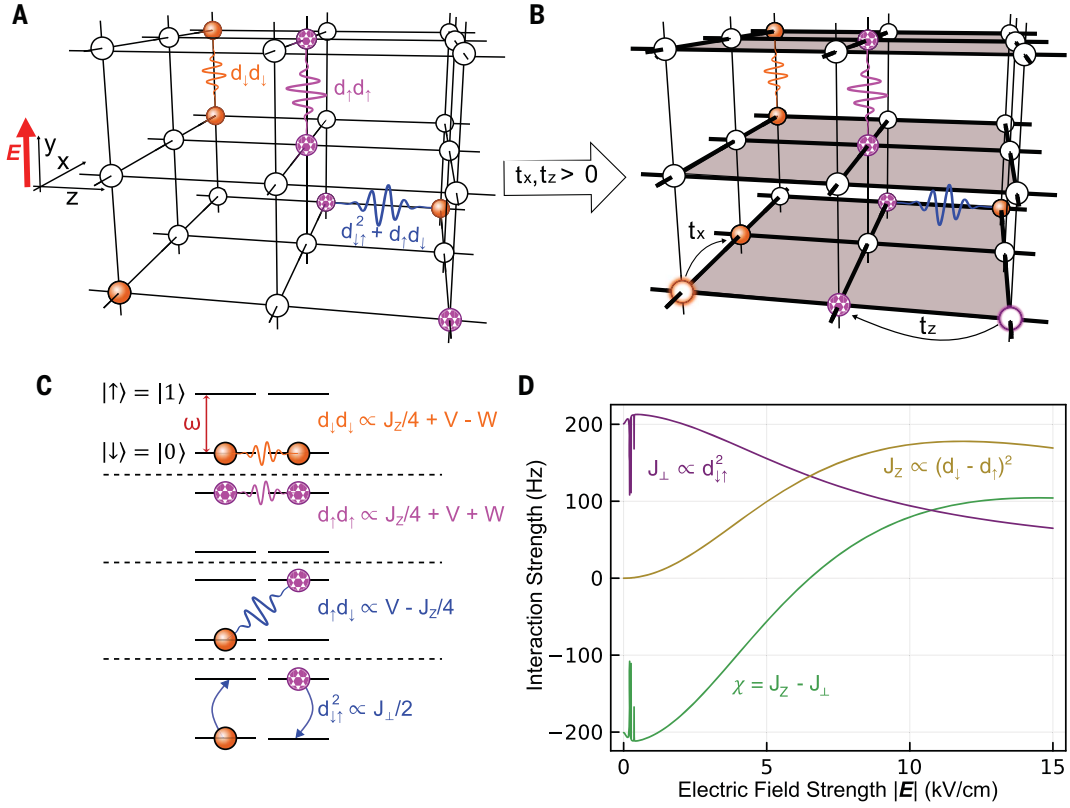

Fig. 1. Field-tunable dipolar interactions between lattice-confined molecules. (**A**) Molecules sparsely occupy a deep 3D optical lattice. Sites are shaded white if unoccupied, pink patterned if in the $|\uparrow\rangle$ state, and solid orange if in the $|\downarrow\rangle$ state. Molecules interact through induced dipole moments and transition dipole moments represented by squiggly lines between lattice sites. (**B**) Lowering the lattice depth in the horizontal directions allows tunneling between sites within layers, represented by the black arrows t_x and t_z. For most of our experiments, $t_x = t_z$. (**C**) Molecular interactions arising from dipole moments can be rewritten in terms of $J_\perp$, J_Z, V, and W, the spin-exchange, Ising, density-density, and spin-density interactions, respectively, which are used in a spin-basis Hamiltonian. The interactions set by $d_\downarrow^2$, $d_\uparrow^2$, $d_\uparrow d_\downarrow$, and $d_{\downarrow\uparrow}^2$, and their associated Hamiltonian terms, are drawn schematically from top to bottom. The two lowest rotational states of the molecules, $|\downarrow\rangle$ and $|\uparrow\rangle$, are split by microwave frequencies ω (red arrow between spin levels in the top row) between 2.2 GHz and 4.2 GHz, depending on electric field strength ($|\boldsymbol{E}|$). (**D**) Calculated dipolar interaction strengths for KRb molecules separated by 532 nm perpendicular to the dipole orientations as a function of $|\boldsymbol{E}|$. Purple represents the spin-exchange interaction $J_\perp$ arising from the transition dipole moment between a $|\downarrow\rangle$ molecule and a $|\uparrow\rangle$ molecule, which decreases with increasing electric field magnitude. Gold represents the Ising interaction J_Z from induced dipole moments, which increases with increasing field strength. Green represents the interaction-type anisotropy $\chi = J_Z - J_\perp$, which crosses zero at around 6.5 kV/cm. Hyperfine structure of the molecules produces interaction strengths that change drastically with small changes in $|\boldsymbol{E}|$ for small electric fields of <1 kV/cm.

where the motion is confined to two dimensions, but the interaction potential remains 3D (*37*). Between these two extremes, both motion and interactions become discretized on a lattice, and the full Hamiltonian reduces to a generalized *t-J* Hamiltonian, the *t-J-V-W* model (*7*, *8*)

$$\hat{H}_{tJVW} = -h\sum_{\langle i,j\rangle,\sigma} t_{ij}\left[\hat{c}_{i\sigma}^\dagger \hat{c}_{j\sigma} + h.c.\right] + h\sum_{i\neq j}\frac{V_{ij}}{2}\left[J_\perp(\hat{\boldsymbol{s}}_i\cdot\hat{\boldsymbol{s}}_j) + \chi\left(\hat{s}_i^Z\hat{s}_j^Z\right) + V\hat{n}_i\hat{n}_j + W\left(\hat{n}_i\hat{s}_j^Z + \hat{n}_j\hat{s}_i^Z\right)\right] + hU\sum_i \hat{n}_{i\downarrow}\hat{n}_{i\uparrow} \quad (2)$$

where $\hat{c}_{i\sigma}^\dagger$ is the fermionic creation operator at lattice site i for spin σ, and we have $\hat{n}_{i\sigma} = \hat{c}_{i\sigma}^\dagger\hat{c}_{i\sigma}$, total site occupation $\hat{n}_i = \sum_\sigma \hat{n}_{i\sigma}$, and magnetization $\hat{s}_i^Z = \left(\hat{c}_{i\uparrow}^\dagger\hat{c}_{i\uparrow} - \hat{c}_{i\downarrow}^\dagger\hat{c}_{i\downarrow}\right)/2$. t_{ij} characterizes the hopping rate of molecules between neighboring sites i and j, denoted $\langle i,j\rangle$. V_{ij} captures the geometric $(1 - 3\cos^2\theta)a_x^3/r^3$ component of the interactions. Strong kilohertz-scale on-site interaction U, rapid on-site two-body loss, and low filling fractions prohibit double occupancy of lattice sites and suppress superexchange interactions. The spin interaction anisotropy χ parameterizes rich spin dynamics that were previously studied at the mean field level (*22*) and produces one-axis twisting that can be used to generate entangled states (*38*, *39*). The $\boldsymbol{E}$-tunability of the interactions for molecules on neighboring lattice sites in the $\hat{x}-\hat{z}$ plane is shown in Fig. 1D. We note that V is spin independent and small compared with spin-spin interactions and thus not expected to appreciably affect the spin dynamics observed here (*36*).

Coherent spin dynamics probed with Ramsey spectroscopy

To explore the out-of-equilibrium coherent dynamics of the molecules in different interaction regimes and geometries of the generalized *t-J* model, we measured the Ramsey contrast decay (Fig. 2A). First, an applied microwave pulse prepared an equal superposition of the $|\downarrow\rangle$ and $|\uparrow\rangle$ states. In a Bloch sphere picture, the collective Bloch vector was prepared along $\hat{X}$ with maximal length $N_{\mathrm{mol}}/2$ for total molecule number N_{mol}. The system was allowed to evolve for a variable time T before a microwave pulse of area $\pi/2$ about variable axis $\hat{R} = \cos\varphi\hat{X} + \sin\varphi\hat{Y}$ was applied. The number of molecules in each spin state was then measured (*36*). By repeating the measurement several times while varying the phase φ of the second pulse and taking the standard deviation of the fraction in the excited state, the contrast, or the equatorial length of the Bloch vector, $C = \frac{2}{N_{\mathrm{mol}}}\sqrt{\left\langle\sum_i \hat{s}_i^X\right\rangle^2 + \left\langle\sum_i \hat{s}_i^Y\right\rangle^2}$ at wait time T was extracted (*36*). Because $\left\langle\sum_i \hat{s}_i^Z\right\rangle = 0$ is conserved during the dynamics, C describes the magnetization of the sample. During T, a KDD pulse sequence (*40*) suppresses single-particle dephasing by frequently swapping the populations in the $|\downarrow\rangle$ and $|\uparrow\rangle$ states (*36*). Dynamical decoupling also removes the W term in the *t-J-V-W* Hamiltonian. The contrast evolution was then fit to a stretched exponential via $C(T) = e^{-(\Gamma T)^\nu}$, where Γ is the dephasing rate and ν is the stretching parameter. We observed $\nu < 1$ for all parameters analyzed in this work, describing subexponential decay, possibly associated with glassy dynamics (*41*) and number loss (*36*).

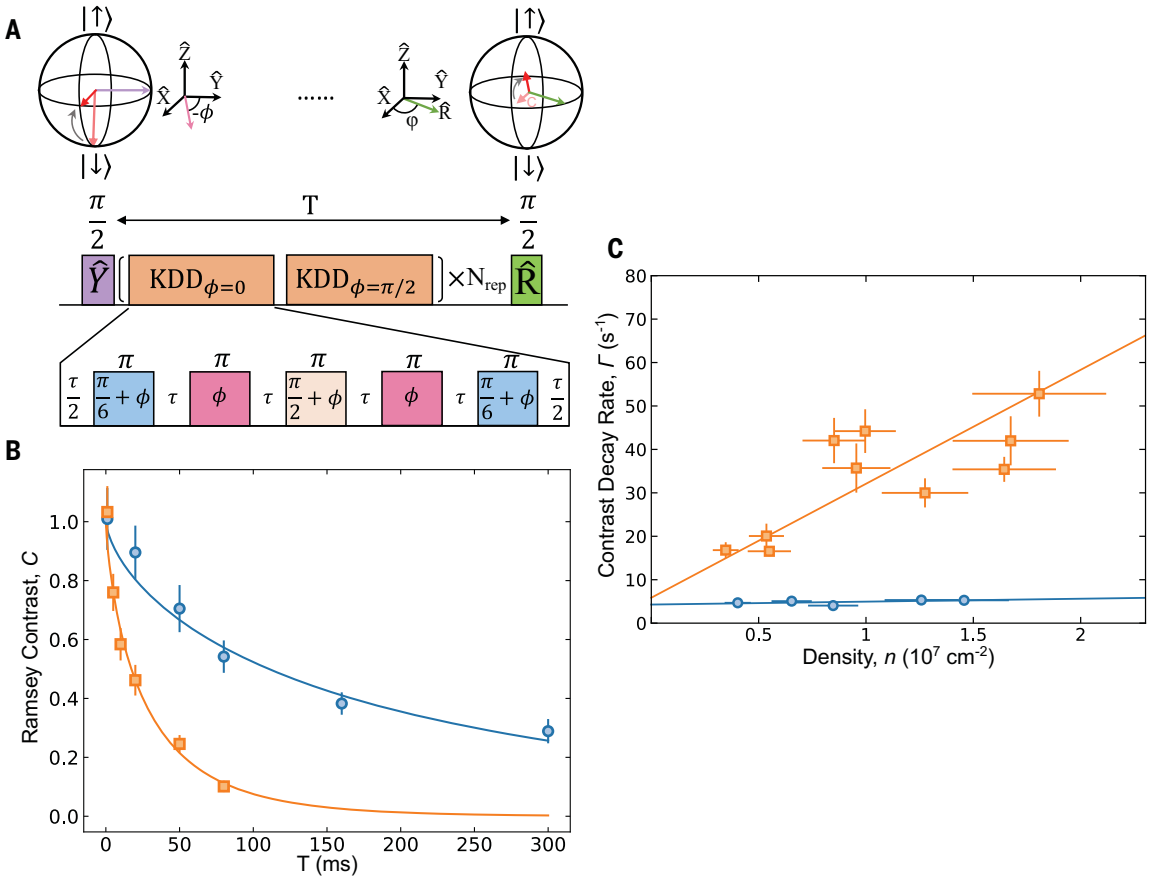

Fig. 2. Dynamical magnetization of interacting pinned molecules. (**A**) Ramsey spectroscopy is used to measure the dynamical magnetization of the molecules. The top row shows the orientation of the collective spin in the Bloch sphere representation, and the middle and bottom rows show the pulse sequence. A $\pi/2$ pulse about the $\hat{Y}$ axis prepares the molecules in a coherent superposition of $1/\sqrt{2}(|\downarrow\rangle + |\uparrow\rangle)$. A KDD pulse sequence (shown as the bottom row) removes single-particle dephasing and is repeated a variable number of times N_{rep} to extend the total interrogation time to T. A final $\pi/2$ pulse about variable axis $\hat{R}$ reads out the projection of the Bloch vector orthogonal to $\hat{R}$. By repeating the measurements varying $\hat{R}$, the equatorial length of the Bloch vector, which is the Ramsey contrast (dynamical magnetization) C, at time T is extracted. (**B**) Measured contrast decay $C(T)$ for $\chi = 0$ (blue circles) and $\chi = 102$ Hz (orange squares) for initial 2D average densities (n) of roughly 1.5×10^7 cm^{-2} of molecules confined in a deep 3D optical lattice. Solid lines are stretched exponential fits to the experimental data. Error bars are 1 SD from bootstrapping (*36*). (**C**) Extracted Ramsey contrast decay rates versus initial density for $\chi = 0$ (blue circles) and $\chi = 102$ Hz (orange squares). Solid lines are linear fits to the data whose slopes measure density-dependent decoherence rate κ. Error bars are 1 SE from fits (stretched exponential fit for contrast decay rates, one-body loss for densities).

To examine the effect of field-tunable interactions on spin coherence, we first froze the motional degree of freedom by confining the molecules in a deep 3D optical lattice ($t_{ij} \approx 0$ in all directions). At zero electric field, $d_\downarrow \approx d_\uparrow \approx 0$, molecules interact predominately through spin exchange, realizing the XY model $\hat{H}_{XY} = h\sum_{i\neq j} \frac{V_{ij}}{2} J_\perp \left(\hat{s}_i^X \hat{s}_j^X + \hat{s}_i^Y \hat{s}_j^Y\right)$. The coherent spin dynamics in this regime at low fillings have been studied (*16*, *17*, *42*), revealing density-dependent Ramsey contrast decay from long-range interactions, with periodic revivals in contrast arising from spin exchange between nearest neighbors. Turning on static $\boldsymbol{E}$ to add Ising interactions realizes the XXZ model $\hat{H}_{XXZ} = h\sum_{i\neq j} \frac{V_{ij}}{2}\left[J_\perp(\hat{\boldsymbol{s}}_i \cdot \hat{\boldsymbol{s}}_j) + \chi\left(\hat{s}_i^Z \hat{s}_j^Z\right)\right]$. Previous works have studied the coherent dynamics of this model in the presence of strong disorder using Floquet engineering on platforms such as nitrogen-vacancy centers in diamond (*43*) and Rydberg atoms (*44*). In this study, we utilized polar molecules to probe these lattice spin models beyond the pure spin-exchange regime. At the Heisenberg point ($\chi = 0$ at $|\boldsymbol{E}| = 6.5$ kV/cm), the Hamiltonian reduces to the isotropic XXX model $\hat{H}_{XXX} = h\sum_{i\neq j} \frac{V_{ij}}{2} J_\perp(\hat{\boldsymbol{s}}_i \cdot \hat{\boldsymbol{s}}_j)$, where the interactions are independent of spin orientation, making all points on the collective Bloch sphere eigenstates of the Hamiltonian. As such, there should be no interaction-induced dephasing. Figure 2B shows contrast decay traces and fits to stretched exponentials for average 2D densities of roughly 1.5×10^7 cm^{-2} at two different values of $\boldsymbol{E}$ where $\chi = 0$ (blue circles) and $\chi = 102$ Hz (orange squares, $|\boldsymbol{E}| = 12.72$ kV/cm). We observed an order of magnitude slower contrast decay at the Heisenberg point than at $\chi = 102$ Hz.

If interactions limit the coherence time, higher densities should lead to faster contrast decay. To extract the effect of many-body processes, the contrast decay measurement was repeated for different initial average 2D densities n (*36*). The contrast decay rates for each n were fit to a linear function $\Gamma(n) = \kappa n + \Gamma_0$, where Γ_0 is the single-particle dephasing rate after dynamical decoupling and κ is the many-body dephasing rate. This density-normalization procedure is shown in Fig. 2C for $\chi = 0$ (blue circles) and $\chi = 102$ Hz (orange squares). Prominently, in the $\chi = 0$ case, we measured $\kappa = 0.07(7) \times 10^{-6}$ cm^2 s^{-1}, consistent with no density-dependent contrast decay, as expected in the XXX model with a single-body dephasing rate, determined from the linear slope offset, of $\Gamma_0 = 4.3(7)$ s^{-1}. By contrast, for $\chi = 102$ Hz, we observed contrast decay rates that depend strongly on density, with $\kappa = 2.6(4) \times 10^{-6}$ cm^2 s^{-1} and $\Gamma_0 = 6(3)$ s^{-1}.

Interaction-limited decoherence dynamics

Repeating the measurement at several values of $|\boldsymbol{E}|$ in the pinned configuration, we observed a roughly linear dependence of κ on $|\chi|$, with a slight dependence on the sign of χ (Fig. 3A). κ depends approximately linearly on $|\chi|$ because dephasing in our lattice originates from couplings with strength proportional to χ within local clusters of molecules. We attribute the observed slower decay in

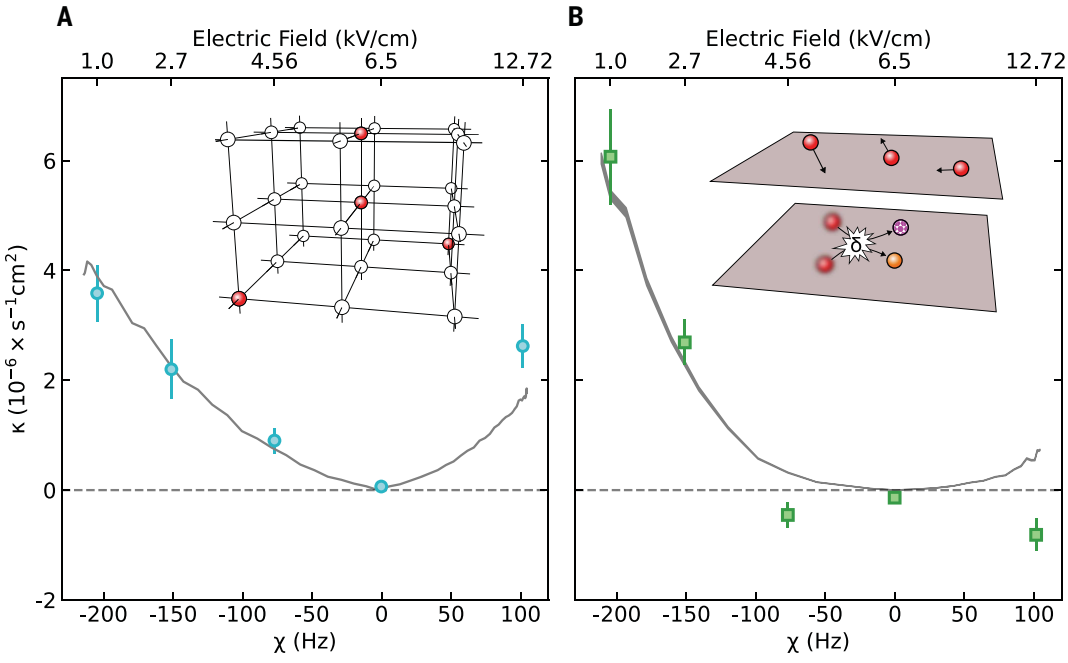

Fig. 3. Field-tunable density-dependent decoherence rates. (**A**) Density-normalized contrast decay rates κ for pinned molecules tuned with interaction anisotropy χ. Blue circles are experimental data extracted from slopes in Fig. 2C. Error bars are 1 SE from linear fits. Gray line is a MACE simulation (*36*) with the same density-normalization procedure as experimental data with no scaling. (Inset) 3D lattice with fully pinned molecules, with white circles representing unoccupied sites and red circles denoting sites occupied by a molecule initially in $1/\sqrt{2}(|\downarrow\rangle + |\uparrow\rangle)$. (**B**) As in (A), but for molecules confined to 2D layers without horizontal corrugation. Green squares are experimental data. Error bars are 1 SE from linear fits. Gray shaded band is from Monte Carlo coherent collision simulations with no scaling (*36*), with the band halfwidth representing 1 SE of linear fit. (Inset) 2D geometry of the system, with molecules (red circles) free to move within 2D layers. In the bottom 2D layer, collisional dephasing occurs when a collision leads to a relative phase shift $\delta = \delta_{\leftrightarrow} - \delta_{\updownarrow}$, making the molecules no longer identical after the collision, illustrated as one molecule becoming pink and the other turning orange.

the $J_\perp$-dominated ($\chi < 0$) regime to periodic self-rephasing from spin exchange within local clusters that is suppressed in the J_Z-dominated ($\chi > 0$) regime (*36*). We also modeled the contrast dynamics using a moving-average cluster expansion (MACE) (*36*, *42*). In this approximation, the dynamics for a given molecule are solved exactly in the presence of its M most strongly coupled neighbors. The global contrast dynamics are then obtained by averaging these "cluster" dynamics for every molecule in the system, with reasonable convergence being obtained for clusters as small as $M = 6$. This convergence for a small particle number is an indicator of the local nature of the spin dynamics under anisotropic dipolar interactions in three dimensions, whereas the spin dynamics for isotropic interactions can depend collectively on all particles in the system in certain geometries (*45*–*47*). The results of the MACE simulation (Fig. 3A, gray trace) show excellent agreement between theory and experiment and confirm that pinned dipolar spin dynamics are well described by the XXZ model.

Next, we observed modifications to the many-body dephasing rates from collisions of fully itinerant molecules. To probe the interplay of motion with spin-dependent dipolar interactions, we confined the molecules to 2D layers formed by a vertical lattice of $65E_r$ depth, where $E_r \approx h \times 1.4$ kHz is the photon recoil energy for KRb. In these experiments, without any horizontal lattice potential ($V_{L,x} = V_{L,z} = 0$), radial harmonic confinement was provided predominantly by a crossed optical dipole trap, which was also maintained for all other experiments. We then extracted the density-normalized dephasing rate κ as a function of χ, as in the pinned molecule case (Fig. 3B, green squares). In prior work (*22*), the short-time mean-field dynamics were well described by an XXZ spin model with spins pinned in a harmonic oscillator mode space lattice (*36*). At longer times relevant for the current measurements, the thermal occupation of our sample enabled molecules to delocalize in mode space caused by mode-changing collisions, invalidating the pinned mode picture. Although collisional decoherence was previously observed in ultracold molecules (*22*), the dependence on dipolar interactions was not completely understood, and modeling dipolar collisional dephasing of coherent superpositions has been challenging.

We systematically measured that κ depends more strongly on $|\chi|$ than in the pinned case, and we present a scattering approach to study the $V_{L,x} = V_{L,z} = 0$ limit of the molecular Hamiltonian to explain our observations. We adopted two methods of theoretical analysis (*36*): collisional Monte Carlo simulations and a simplified analytic model. Data obtained from Monte Carlo simulations (Fig. 3B, gray trace) show agreement with the experimental data, apart from experimentally measured negative values of κ. We attribute these negative values to the preferential two-body loss of decohered molecules (*36*). The agreement between theory and experiment suggests that our theoretical model captures the relevant physics from collisional dephasing of molecular superpositions.

The simplified analytic model provides a more intuitive understanding of the observed stronger, approximately cubic dependence of κ on $|\chi|$. With the molecular spins initially prepared in the state $|X\rangle = (|\uparrow\uparrow\rangle + |\downarrow\downarrow\rangle + |\uparrow\downarrow\rangle + |\downarrow\uparrow\rangle)/2$, their first collision would only involve states in the symmetric spin sector: $|\downarrow\downarrow\rangle$, $(|\uparrow\downarrow\rangle + |\downarrow\uparrow\rangle)/\sqrt{2}$, and $|\uparrow\uparrow\rangle$, which each accrue a scattering phase shift. Collisions in this sector are predominantly elastic, as Fermi statistics suppresses close contact of the molecules, implying that long-ranged dipolar interactions dominate these phase shifts. We therefore expect that completed collisions are slow compared with the dynamical decoupling pulses that rapidly flip molecules between $|\downarrow\rangle$ and $|\uparrow\rangle$. The result is that the aligned $(\updownarrow)|\downarrow\downarrow\rangle$ and $|\uparrow\uparrow\rangle$ spin states will both incur the same scattering phase shift $\delta_\updownarrow$ proportional to dipole length (*48*): $a_D^{\updownarrow} \propto d_\downarrow^2 + d_\uparrow^2 \propto V + \frac{J_\perp}{4} + \frac{\chi}{4}$. The remaining anti-aligned triplet state ($\leftrightarrow$) will, in general, develop a different phase shift $\delta_\leftrightarrow$ proportional to the dipole length $a_D^{\leftrightarrow} \propto d_{\downarrow\uparrow}^2 + d_\downarrow d_\uparrow \propto V + \frac{J_\perp}{4} - \frac{\chi}{4}$. Each single collision thus causes the scattered molecules to decohere, with a change in contrast $\Delta C = 2\sin^2(\delta_\leftrightarrow - \delta_\updownarrow) \propto \chi^2$ for small $\delta_\leftrightarrow - \delta_\updownarrow \propto \chi$ (see inset of Fig. 3B for schematic). The total dephasing rate is approximated by the product of the change in contrast for each collision and the elastic collision rate:

$\kappa \propto \Delta C \beta_{el}$. For 2D motion, ultracold identical spin-polarized fermionic molecules scatter elastically at a rate proportional to their threshold cross section $\sigma \approx 8\pi k a_D^2$, where k is the relative momentum of the colliding pair (*23*, *37*, *48*). Molecules in superpositions should also elastically scatter from both aligned and anti-aligned channels, so that $\beta_{el} = (\beta_{\updownarrow} + \beta_{\leftrightarrow})/2 = 4\pi\hbar k^2 \left[\left(a_D^{\updownarrow}\right)^2 + \left(a_D^{\leftrightarrow}\right)^2\right]/\mu$, where μ is the reduced mass of the pair. Evaluating the product for κ captures the dominant $\kappa \propto |\chi|^3$ scaling seen to arise in the Monte Carlo simulations (*36*). Notably, we find that this scaling is sensitive to the trap frequency of the tight confining axis and is thus relevant to our current experiment but not universal.

Spin dynamics of the generalized *t-J* model

We next explored the more complex generalized *t-J* model regime by tuning tunneling within 2D layers. Experimentally, we studied the effect of motion on contrast by measuring κ of molecules confined in a deep vertical lattice with variable corrugation in the $\hat{x}$ and $\hat{z}$ directions, for different values of χ. The measured values of κ as a function of tunneling rate t in both the $\hat{x}$ and $\hat{z}$ directions are plotted in Fig. 4A, with black circles, blue squares, and orange triangles representing χ = −205, 0, and 102 Hz ($J_\perp$ = 211, 133, and 75 Hz), respectively. For χ = 0 Hz, we observed no density-dependent contrast decay (that is, κ was consistent with 0) over the entire range of t explored, as intuitively expected at the Heisenberg point. For χ = 102 Hz, we saw a smooth transition between the two motional extremes, with κ gradually decreasing for increasing t. For χ = −205 Hz, we observed stronger decoherence in general, with a peak in decoherence rate around t = 70 Hz. Similar to the fully itinerant case, and as a result of the nonlinear dependence of collisional dephasing on $|\chi|$, it is not surprising that the behavior for χ = −205 Hz can be qualitatively different than for χ = 102 Hz.

To understand the observed peak when χ = −205 Hz, we first examined the rise in κ as the lattice depth was reduced from the pinned molecule case. Intuitively, increasing tunneling will couple the internal and external degrees of freedom of the molecules, leading to increased dephasing. This mechanism is well captured by simulations with an extended MACE (EMACE) (*36*), which adds molecular motion to the standard MACE and is shown as a light gray (orange) band for χ = −205 Hz (χ = 102 Hz) in Fig. 4A.

We next examined the enhanced contrast decay as the lattice depth was increased from zero. From a band structure perspective, increasing the lattice depth shrinks the width of each motional band, increasing its density of states and allowing more channels for mode-changing collisions, generally leading to faster spin decoherence (*36*) (Fig. 4B). From a scattering perspective, in the lattice, molecules

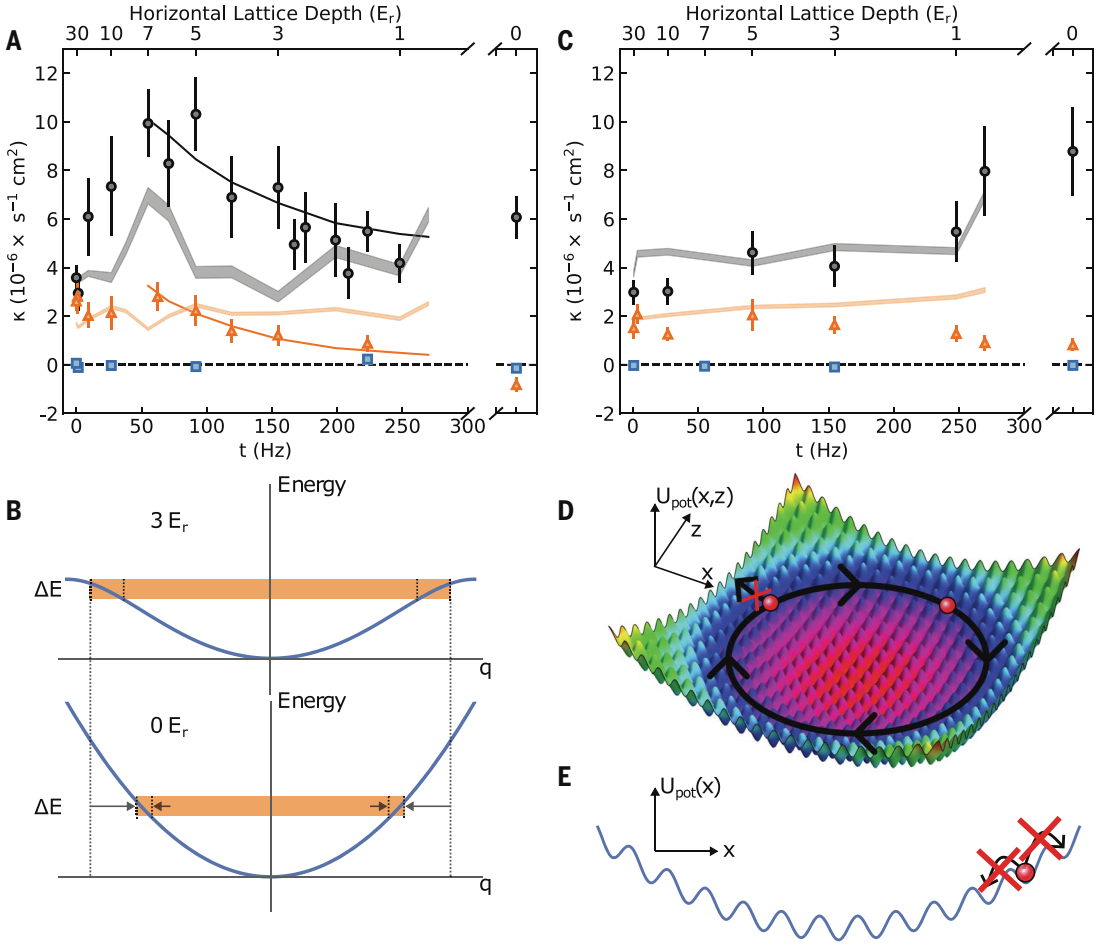

Fig. 4. Tuning coherent *t-J* dynamics. (**A**) Density-dependent contrast decay rates κ versus tunneling rate t in two directions. Black circles, blue squares, and orange triangles represent experimental data for χ = −205, 0, and 102 Hz, respectively. Horizontal axis break occurs when transverse lattices are turned off (case of Fig. 3B). Error bars are 1 SE from linear fits. Light gray (orange) bands are EMACE simulations (*36*) for χ = −205 Hz (χ = 102 Hz) with no scaling, with the band halfwidth representing 1 SE of linear fit. Black (orange) solid lines shown for t > 50 Hz are two-body simulations (*36*) with a rescaling by 0.75 for χ = −205 Hz (χ = 102 Hz). (**B**) (Top row) Kinetic energy of two particles in a $3E_r$ lattice as a function of relative quasi-momentum q. (Bottom row) Kinetic energy in the absence of a lattice where $q = k$. Shaded orange regions show the range of momentum states within a given energy interval, showing the increased density of states in a shallow lattice compared with the no-lattice case. (**C**) As in (A), but for tunneling only in one direction. (**D**) 3D rendering of the single-molecule potential energy U_{pot} in the $\hat{x}$ and $\hat{z}$ directions arising from a weak 2D optical lattice and a crossed optical dipole trap. Colors indicate equipotential surfaces. Because of the site-to-site energy shift, molecular tunneling along the radial directions is suppressed, and tunneling instead occurs along azimuthal rings. (**E**) Schematic of the localization of molecules within a potential landscape U_{pot} produced by a weak 1D optical lattice in the $\hat{x}$ direction and a crossed optical dipole trap [equivalently, by taking a 1D slice of the 2D lattice potential shown in (D)] because of site-to-site energy shifts, when the motion is also frozen in the other two directions by deep optical lattices.

move slower because of larger effective mass (*49*), increasing the phase shifts accrued in each collision, enhancing contrast decay. In addition, molecular losses from inelastic collisions increase as the lattice depth is reduced (*36*), and the losses are largest for molecules that have already decohered, suppressing contrast decay in the remaining sample (*36*). While the EMACE simulation qualitatively captures the peak structure, quantitative differences arise owing to neglected molecular loss and limited cluster sizes. To further understand the role of mode-changing collisions and molecular loss in shallow lattices, a two-body simulation based on Hamiltonian trotterization (*36*) is included for $t > 50$ Hz as a black (orange) solid line for $\chi = -205$ Hz ($\chi = 102$ Hz) in Fig. 4A, which agrees well with the experimental data with an empirical rescaling of 0.75.

Finally, we studied the role of motional dimensionality on the spin dynamics by measuring the dependence of κ on t for molecules allowed to tunnel in only one direction (Fig. 4C). Whereas the $\chi = 0$ Hz and $\chi = 102$ Hz dynamics are almost identical to the 2D case, the peak in contrast decay around $t \approx 70$ Hz for $\chi = -205$ Hz disappears when the kinetic dimensions are reduced from two to one. In one dimension, we instead only observed a rise in κ at very shallow lattices ($t \gtrsim 200$ Hz). We attribute the different $\chi = -205$ Hz dynamics in the 1D case to the interplay of the confining harmonic trap with the lattice. For tunneling in only one direction, the combined potential leads to quasi-localization of the molecules owing to potential energy differences between neighboring lattice sites (*50*, *51*), schematically shown in Fig. 4E. In the 1D configuration, most of the molecules are localized along all three axes of motion (*36*), leading to dynamics qualitatively similar to the motionless case as the lattice depth is lowered. In contrast, for the 2D case, the additional tunneling dimension allows these particles to delocalize within a quasi-1D azimuthal ring (Fig. 4D).

An EMACE simulation [gray (orange) band for $\chi = -205$ Hz ($\chi = 102$ Hz)] in Fig. 4C shows favorable agreement with experimental values of κ as t is varied in one direction. Note that the number of available tunneling sites is smaller in one dimension than in two, enabling more-controlled EMACE simulations for shallow lattices in the 1D case than in the 2D case (*36*). As shown in both the experimental data and EMACE simulations, the 1D dynamics remain relatively flat between the pinned and fully itinerant cases, consistent with the quasi-localization picture. We attribute the slight disagreement between theory and experiment at very shallow lattices ($t \gtrsim 200$ Hz) for $\chi = 102$ Hz to molecular loss not included in EMACE and to the breakdown of the single-band tight-binding model.

Discussion and outlook

Here, we present a systematic study of the out-of-equilibrium dynamics of a generalized *t-J* system of interacting polar molecules. By increasing molecular filling fractions and using single-site detection (*6*, *17*) or spectroscopic signatures (*52*, *53*), it should be possible to study equilibrium states of these dipolar Hamiltonians. Using similar experimental techniques, a future out-of-equilibrium investigation could probe spin diffusion in lattice-confined polar molecules, potentially observing many-body localized states (*54*). Additionally, with an isolated single layer (*18*) and improved detection, the generalized *t-J* model is predicted to dynamically generate highly entangled spin-squeezed states with applications to precision measurement (*38*, *39*). Recently, we demonstrated Floquet engineering of XYZ spin models, including a two-axis twisting Hamiltonian (*55*), which could enable more-scalable spin squeezing than that produced with native XXZ models. Ultracold molecules, whose dipolar interactions can be tuned independently of motion, have thus emerged as a versatile platform to study a broad range of itinerant spin problems in many-body physics.

REFERENCES AND NOTES

1. P. A. Lee, N. Nagaosa, X.-G. Wen, *Rev. Mod. Phys.* **78**, 17–85 (2006).
2. B. Keimer, S. A. Kivelson, M. R. Norman, S. Uchida, J. Zaanen, *Nature* **518**, 179–186 (2015).
3. P. W. Anderson, *Science* **235**, 1196–1198 (1987).
4. U. Schneider *et al*., *Science* **322**, 1520–1525 (2008).
5. D. Greif, T. Uehlinger, G. Jotzu, L. Tarruell, T. Esslinger, *Science* **340**, 1307–1310 (2013).
6. A. Mazurenko *et al*., *Nature* **545**, 462–466 (2017).
7. A. V. Gorshkov *et al*., *Phys. Rev. Lett.* **107**, 115301 (2011).
8. A. V. Gorshkov *et al*., *Phys. Rev. A* **84**, 033619 (2011).
9. L. Chomaz *et al*., *Rep. Prog. Phys.* **86**, 026401 (2022).
10. L. Su *et al*., *Nature* **622**, 724–729 (2023).
11. A. de Paz *et al*., *Phys. Rev. Lett.* **111**, 185305 (2013).
12. P. Fersterer *et al*., *Phys. Rev. A* **100**, 033609 (2019).
13. S. Baier *et al*., *Science* **352**, 201–205 (2016).
14. A. Patscheider *et al*., *Phys. Rev. Res.* **2**, 023050 (2020).
15. Y. Tang *et al*., *Phys. Rev. X* **8**, 021030 (2018).
16. B. Yan *et al*., *Nature* **501**, 521–525 (2013).
17. L. Christakis *et al*., *Nature* **614**, 64–69 (2023).
18. W. G. Tobias *et al*., *Science* **375**, 1299–1303 (2022).
19. C. M. Holland, Y. Lu, L. W. Cheuk, *Science* **382**, 1143–1147 (2023).
20. Y. Bao *et al*., *Science* **382**, 1138–1143 (2023).
21. P. D. Gregory *et al*., *Nat. Phys.* **20**, 415–421 (2024).
22. J.-R. Li *et al*., *Nature* **614**, 70–74 (2023).
23. G. Valtolina *et al*., *Nature* **588**, 239–243 (2020).
24. A. Schindewolf *et al*., *Nature* **607**, 677–681 (2022).
25. N. Bigagli *et al*., *Nature* **631**, 289–293 (2024).
26. L. Anderegg *et al*., *Science* **373**, 779–782 (2021).
27. J. Lin *et al*., *Phys. Rev. X* **13**, 031032 (2023).
28. A. V. Avdeenkov, *Phys. Rev. A* **86**, 022707 (2012).
29. L. Lassablière, G. Quéméner, *Phys. Rev. Lett.* **121**, 163402 (2018).
30. T. Karman, J. M. Hutson, *Phys. Rev. Lett.* **121**, 163401 (2018).
31. K. Matsuda *et al*., *Science* **370**, 1324–1327 (2020).
32. J.-R. Li *et al*., *Nat. Phys.* **17**, 1144–1148 (2021).
33. G. Quéméner, J. L. Bohn, *Phys. Rev. A* **93**, 012704 (2016).
34. M. L. González-Martínez, J. L. Bohn, G. Quéméner, *Phys. Rev. A* **96**, 032718 (2017).
35. B. Mukherjee, M. D. Frye, C. R. Le Sueur, M. R. Tarbutt, J. M. Hutson, *Phys. Rev. Res.* **5**, 033097 (2023).
36. Materials and methods are available as supplementary materials.
37. G. Quéméner, J. L. Bohn, *Phys. Rev. A* **83**, 012705 (2011).
38. T. Bilitewski *et al*., *Phys. Rev. Lett.* **126**, 113401 (2021).
39. D. Wellnitz, M. Mamaev, T. Bilitewski, A. M. Rey, *Phys. Rev. Res.* **6**, L012025 (2024).
40. A. M. Souza, G. A. Álvarez, D. Suter, *Phys. Rev. Lett.* **106**, 240501 (2011).
41. A. Signoles *et al*., *Phys. Rev. X* **11**, 011011 (2021).
42. K. R. A. Hazzard *et al*., *Phys. Rev. Lett.* **113**, 195302 (2014).
43. L. S. Martin *et al*., *Phys. Rev. Lett.* **130**, 210403 (2023).
44. S. Geier *et al*., *Science* **374**, 1149–1152 (2021).
45. M. P. Kwasigroch, N. R. Cooper, *Phys. Rev. A* **96**, 053610 (2017).
46. M. Block *et al*., *Nat. Phys.* **20**, 1575–1581 (2024).
47. M. A. Perlin, C. Qu, A. M. Rey, *Phys. Rev. Lett.* **125**, 223401 (2020).
48. C. Ticknor, *Phys. Rev. A* **80**, 052702 (2009).
49. N. W. Ashcroft, N. D. Mermin, *Solid State Physics* (Holt, Rinehart and Winston, 1976).
50. M. Rigol, A. Muramatsu, *Phys. Rev. A* **70**, 043627 (2004).
51. A. M. Rey, G. Pupillo, C. W. Clark, C. J. Williams, *Phys. Rev. A* **72**, 033616 (2005).
52. J. T. Stewart, J. P. Gaebler, D. S. Jin, *Nature* **454**, 744–747 (2008).
53. H.-J. Shao *et al*., arXiv:2402.14605 [cond-mat.quant-gas] (2024).
54. N. Y. Yao *et al*., *Phys. Rev. Lett.* **113**, 243002 (2014).
55. C. Miller *et al*., *Nature* **633**, 332–337 (2024).
56. A. N. Carroll *et al*., Data for "Observation of Generalized t-J Spin Dynamics with Tunable Dipolar Interactions" [Data set], Zenodo (2025); https://doi.org/10.5281/zenodo.14941807.

ACKNOWLEDGMENTS

We thank N. Darkwah Oppong and A. V. Gorshkov for a careful review of this manuscript and for providing useful comments. We acknowledge experimental contributions from J.-R. Li and J. S. Higgins and helpful discussions with P. J. D. Crowley and N. Y. Yao. **Funding:** This material is based on work supported by National Science Foundation grant QLCI OMA-2016244. Additional support is acknowledged from the US Department of Energy, Office of Science, National Quantum Information Science Research Centers, Quantum Systems Accelerator; ARO and AFOSR MURIs; JILA Physics Frontier Center grant PHY-2317149; National Science Foundation grant PHY-2110327; ARO single investigator award W911NF-24-1-0128; and the National Institute of Standards and Technology. A.N.C. acknowledges support from the National Science Foundation Graduate Research Fellowship under grant DGE 2040434. C.M. acknowledges support from the US Department of Defense through the NDSEG Graduate Fellowship. S.R.M. acknowledges support from the National Science Foundation under grant QLCI OMA-2120757. K.P.Z. acknowledges support from the Austrian Science Fund (FWF) under grant W1259-N27. R.R.W.W. acknowledges partial support from the National Science Foundation through a grant from ITAMP at Harvard University. **Author contributions:** A.N.C., H.H., C.M., J.L., K.P.Z., and J.Y. conducted the experiments and analyzed the data. D.W., S.R.M., R.R.W.W., J.L.B., and A.M.R. developed the theoretical models. All authors contributed to interpreting results and writing the manuscript. **Competing interests:** The authors declare that they have no competing interests. **Data and materials availability:** All data needed to evaluate the conclusions in this paper are available in Zenodo (*56*).

SUPPLEMENTARY MATERIALS

science.org/doi/10.1126/science.adq0911
Materials and Methods
Supplementary Text
Figs. S1 to S16
Table S1
References (*57*–*73*)

Submitted 25 April 2024; accepted 27 February 2025
10.1126/science.adq0911